Supplemental Material

for

"Local homeostasis preserves global neural dynamics compensating for structural loss during human lifespan aging"

Suman Saha[1,2*], Priyanka Chakraborty[1,3*], Amit Naskar[1], Dipanjan Roy[4*], Arpan Banerjee[1*]

[1]Cognitive Brain Dynamics Lab, National Brain Research Centre, NH 48, Gurgaon, 122052, Haryana, India.

[2]School of Engineering, Vellore Institute of Technology, Kelambakkam-Vandalur Rd, Rajan Nagar, Chennai, 600127, Tamil Nadu, India.

[3]Department of Mathematics, Rampurhat College, Dackbanglow More, Rampurhat, 731224, West Bengal, India.

[4]School of AIDE, Center for Brain Research and Applications, Indian Institute of Technology, NH 62, Nagaur Road, Jodhpur, 342037, Rajasthan, India.

*Corresponding author(s). E-mail(s): ecesuman06@gmail.com; priya.chakraborty18@gmail.com; droy@iitj.ac.in; arpan@nbrc.ac.in;

Contents

1 Descriptions of the three datasets

1.1 CamCAN dataset

1.1.1 Subjects

In our study, total 69 healthy participants were included from the Cambridge Centre for Ageing and Neuroscience (CamCAN) cohort http://www.mrc-cbu.cam.ac.uk/datasets/camcan/http://www.mrc-cbu.cam.ac.uk/datasets/camcan/ Shafto et al (2014); Taylor et al (2017).

1.1.2 Data acquisition

Resting state MRI (T1-weighted image), diffusion weighted MRI, and functional MRI were performed using a 3T Siemens TIM Trio scanner with a 32-channel head-coil at Medical Research Council (UK) Cognition and Brain Sciences Unit (MRC-CBSU) in Cambridge, UK.

High-resolution 3D T1-weighted data was collected with a magnetization prepared rapid gradient echo (MPRAGE) sequence using Generalized Auto-calibrating Partially Parallel Acquisition (GRAPPA) with acceleration factor of 2 and other parameters were: repetition time (TR)=2,250 ms, echo time (TE)=2.99 ms, flip angle: 9°, field of view (FOV)=256 × 240 × 192 mm; voxel size = 1 mm^3 isotropic, inversion time (TI)=900 ms, acquisition time (TA)=4:32min Shafto et al (2014).

Diffusion data were acquired in a twice-refocused spin echo sequence with TR of 9100 ms, TE of 105 ms, FOV of 192 × 192 mm, isotropic voxel size of 2 mm^3, 66 axial slices using 30 directions with b = 1000 s/mm^2, 30 directions with b = 2000 s/mm^2, and three b = 0 images with single average Shafto et al (2014). Resting state eye closed fMRI was collected with EPI sequence with 1970 ms TR, 30ms TE, 78° flip angle, 192 × 192 mm FOV, 3 × 3 × 4.44 mm^3 voxel size, 32 slices of thickness 3.7 mm Shafto et al (2014).

1.1.3 DTI processing

Diffusion MRI data were processed locally using own pre-processing pipeline by using MRtrix3 (Tournier et al (2019),
https://github.com/MRtrix3/mrtrix3https://github.com/MRtrix3/mrtrix3), FSL
http://www.fmrib.ox.ac.uk/fsl
http://www.fmrib.ox.ac.uk/fsl, and ANTS http://stnava.github.io/ANTs/, http://stnava.github.io/ANTs/. Main preprocessing steps include denoising (MRtrix command 'dwidenoise', Veraart et al (2016)), Gibb's ringing artefacts removal (MRtrix command 'mrdegibbs', Kellner et al (2016)), motion and eddy current corrections (MRtrix command 'dwifslpreproc', Andersson et al (2003)), biasness corrections (MRtrix command 'dwibiascorrecT using ANTs, Tustison et al (2010)). Then a brain mask in DTI space was calculated for each subject using 'beT command (in FSL) on the preprocessed image. To find the orientation of the fiber(s) (fiber orientation distribution, FOD) in each voxel, we used multi-shell multi-tissue constrained spherical deconvolution (MSMT-CSD; MRtrix command 'dwi2response' and 'dwi2fod', Dhollander et al (2018)). After that, a global intensity normalization has been performed to make the fiber orientation distributions comparable between subjects. We used Anatomically Constrained Tractography (ACT, MRtrix

command '5ttgen', Smith et al (2012)) to generate a tissue-segmented image. In order to use ACT, we first preprocess the T1-weighted image using MRtrix, then we co-registered that image to the DWI using both MRtrix and FSL. We created an mask of the gray-matter/white-matter-boundary, which was useful for streamline seeding. Finally, probabilistic tractography (MRtrix command 'tckgen') has been used to generate 20 million tracks. The tractogram was filtered (SIFT2 approach, MRtrix command 'tcksift2') further to a find subset of streamlines such that the streamlines densities were more close to fibre densities Smith et al (2015). Each steps were visually assessed and edited by research personnel.

1.1.4 T1 processing

Freesurefer http://surfer.nmr.mgh.harvard.eduhttp://surfer.nmr.mgh.harvard.edu Dale et al (1999) 'recon-all' used to reconstruct a two-dimensional cortical surface from a three-dimensional volume acquired from T1-weighted image. Recon-all steps were skull stripping from the anatomical image, estimation of interface between the white matter and grey matte, generation of white and pial surfaces. Cortical parcellation was performed using the Desikan-Killiany (DK) atlas Desikan et al (2006), with 68 ROIs.

1.1.5 Structural connectivity

A Desikan–Killiany (DK) atlas based whole-brain connectome was generated for each subjects by computing the fiber density between each pair of ROIs (MRtrix command 'tck2connectome' with option 'scale_invnodevol') to count how many streamlines from one region reach every other regions.

1.1.6 fMRI preprocessing using Desikan–Killiany atlas

Functional MRI (fMRI) images for resting state has been preprocessed using CONN toolbox Whitfield-Gabrieli and Nieto-Castanon (2012) https://web.conn-toolbox.org/https://web. conn-toolbox.org/, a Matlab/SPM-based software. Data were preprocessed using a default preprocessing pipeline of CONN. The preprocessing methods were unwrapping using field-map images, realignment to correct for motion, slice timing correction, segmentation, normalisation to the MNI template, outlier rejection and functional smoothing. Spatial smoothing was performed using a Gaussian kernel with full width of 12 mm. Denoising was used to remove signal changes related to white matter, cerebrospinal fluid, motion, breathing and cardiac pulsations. Finally temporal band-pass filtering at (0.004-0.1 Hz) and linear detrending were performed. For region of interest (ROI) analysis, mean regional BOLD time series were estimated in 68 parcellated brain areas of Desikan–Killiany atlas Desikan et al (2006).

1.1.7 Resting state functional connectivity using Desikan–Killiany atlas

The same participants were subjected to a functional MRI (fMRI) scan during which their eyes-closed awake resting-state data were acquired. The resting-state BOLD activity was recorded for 22 minutes (TR=1.97 sec). The BOLD activity was then down-sampled to fit the 68 ROIs. Aggregated BOLD time series of each region were z-transformed. Next, pairwise Pearson correlation coefficient were computed to obtain 68×68 rsFC matrix for individual subjects.

1.2 NKI/Rockland data set:

We tested our hypothesis on another human neuroimaging dataset obtained from Nathan Kline Institute (NKI)/Rockland sample (available in the UCLA Multimodal Connectivity Database (UMCD)Brown et al (2012).

1.2.1 Structural connectivity

Diffusion Tensor Imaging (DTI) based structural connectivity matrices and rsFC/Pearson correlation matrix of 75 healthy participants were obtained from the Nathan Kline Institute (NKI), Rockland sample Brown et al (2012). The participants consisted of 30 males and 35 females, with a total age range of 19-85 (mean $\pm$ std). We separate 40 participants into two age groups (48 young and 27 old) and averaged their SCs over individual subject for our analysis (see Table 1). Cortical gray matter was parcellated using the Craddock 200 atlas Craddock et al (2012). Elements of the SC represented the number of white matter tracts between gray matter parcels. The reader may also refer to the original work Brown et al (2012) for details regarding structural and functional connectome pre-processing. Prior to running the models on the NKI

SC, the SC was scaled down by dividing every element by the maximum value found in the original SC consisting of white matter tract numbers between regions. Diffusion tensors were estimated using Diffusion Toolkit (http://trackvis.org/blog/tag/diffusion-toolkit) and tractography was run using the fiber assignment by continuous tracking algorithm Mori and Van Zijl (2002). For each ROI, all fibers were counted that intersected at least one voxel in the source ROI and at least one voxel in any target ROI using custom code, (http://ccn.ucla.edu/wiki/index.php/UCLA_Multimodal_Connectivity_Package). Thus, 188×188 structural connectivity was obtained.

1.2.2 Resting-state functional connectivity using Craddock-200 atlas

Resting state fMRI data was pre-processed using the pipeline described in Brown et al (2012). After marking flagged TRs, the mean time series for each ROI was calculated and then correlated with all remaining ROI time series (excluding flagged TRs) to derive a 188×188 resting-state functional connectivity (rsFC) matrix parcellated using the Craddock-200 atlas Craddock et al (2012).

1.2.3 Resting-state functional connectivity using AAL parcellation

We have performed every analysis in NKI dataset using Craddock atlas; only metastability is measured using the AAL atlas to maintain consistency with the CamCAN analyses, where we also examined the metastability metric using AAL atlas (116 ROIs), besides Desikan–Killiany atlas (see section 2.4.3, Fig. S4 for CamCAN results using AAL atlas). This served as a cross-validation of the metastability metric. Since metastability is a time-varying measure, qualitatively similar results are obtained whether we use Desikan (68 ROIs) or the AAL atlas (116 ROIs).

Functional MRI images for resting state have been preprocessed using the CONN toolbox Whitfield-Gabrieli and Nieto-Castanon (2012) https://web.conn-toolbox.org/https://web. conn-toolbox.org/, a Matlab/SPM-based software. Data were preprocessed using a default preprocessing pipeline of CONN. The preprocessing methods were unwrapping using field-map images, realignment to correct for motion, slice timing correction, segmentation, normalisation to the MNI template, outlier rejection and functional smoothing. Spatial smoothing was performed using a Gaussian kernel with full width of 2 mm, and TR=2.5 sec. Denoising was used to remove signal changes related to white matter, cerebrospinal fluid, motion, breathing and cardiac pulsations. Temporal band-pass filtering at (0.004-0.1 Hz) and linear detrending were performed. Mean regional BOLD time series were estimated in 115 brain areas of AAL atlas Tzourio-Mazoyer et al (2002). We used the preprocessed BOLD signals in NKI dataset for metastability analysis only, presented in the main text Fig. 2.

1.3 Berlin data

1.3.1 Subjects

The study included 36 healthy subjects (22 females, 14 males). The written consent from the participants are taken care by Schirner et al (2015). The earlier study Schirner et al (2015) was approved by ethics committee of the Charité University Berlin, and all experiments were performed in compliance with the relevant laws and institutional guidelines. We divided 41 subjects into two age groups comprising 22 young participants ranged in age range 18-33 years (mean age=25.68 ± 4 years, 13 female) and 16 elderly participants of age range 55-80 years (mean age=65.06 ± 7.39 years, 11 female).

1.3.2 Data Acquisition

T1 structural magnetic resonance images (MRI) and diffusion-weighted images (DWI) were acquired at Berlin Center for Advanced Imaging, Charité University Medicine, Berlin, Germany. MRI was performed on a 3T Siemens Trim Trio scanner and a 12 channel Siemens head coil (voxel size). Structural (T1-weighted high-resolution three-dimensional MPRAGE sequence; TR=1900ms, TE=2.52ms, TI=900ms, flip angle=9°, field of view (FOV)=256mm×256mm×192mm, 256 × 256 × 192 matrix, 1.0mm isotropic voxel resolution), diffusion-weighted (T2-weighted sequence; TR=7500ms, TE=86ms, FOV = 192mm × 192mm, 96×96 matrix, 61 slices, 2.3mm isotropic voxel resolution, 64 diffusion directions), and fMRI data (2-dimensional T2-weighted gradient echo planar imaging blood oxygen level-dependent contrast sequence; TR=1940ms, TE=30ms, flip angle=78°, FOV=192 × 192mm^2, 3 × 3mm^2 voxel resolution, 3mm slice thickness, 64 × 64

matrix, 33 slices, 0.51ms echo spacing, 668 TRs, 7 initial images were acquired and discarded to allow magnetization to reach equilibrium; eyes-closed resting-state) were acquired on a 12-channel Siemens 3 Tesla Trio MRI scanner at the Berlin Center for Advanced Neuroimaging, Berlin, Germany.

1.3.3 Structural connectivity

The structural connectivity (SC) for each subject and age is generated using the pipeline described by Schiner et. al. Schirner et al (2015). In the pipeline, high-resolution T1 anatomical images were used to create segmentation and parcellation of cortical and sub-cortical gray matter, white matter segments. The main pre-processing steps for T1 anatomical images involved skull stripping, removal of non-brain tissue, brain mask generation, cortical reconstruction, motion correction, intensity normalization, WM, and subcortical segmentation, cortical tessellation generating GMWM and GM-pia interface surface-triangulation and probabilistic atlas-based cortical and subcortical parcellation. Cortical grey matter parcellation of 34 region of interest (ROI) in each hemisphere was undertaken following Desikan-Killiany parcellation Desikan et al (2006). The connection strength (a value ranging from 0 to 1) between each pair of ROIs was estimated by probabilistic tractography algorithm. SC matrices were generated from each subject's MRI data and then summed element-wise to obtain an averaged SC matrix. The pre-processing steps for the diffusion MRI data were eddy current and motion correction with re-orientation of b-vectors (b-zero image was linearly registered to the subject's anatomical T1-weighted image). Tractography was constrained by seed, target, and stop masks. The fiber length was represented in millimeters. The 68 ROIs or nodes had no self-connection loops meaning that the diagonal values of the SC matrix are all zero.

1.3.4 Resting state functional connectivity

The participants were subjected to a functional MRI scan, when eyes-closed awake resting-state data were acquired. The resting-state BOLD activity was recorded for 22 minutes (TR=2 sec) using a 3T Siemens Trim Trio scanner, and a 12 channel Siemens head coil (voxel size). The BOLD signal was computed for 68 ROIs, parcellated by Desikan-Killiany atlas Desikan et al (2006) and z-transformed. Pearson correlation coefficient, between each pair of region, defines resting-state FC matrix.

Table S1 Demographic data across two different stages of adulthood in men and women.

Data set	Group	Young Number/mean±sd	Old Number/mean±sd
CamCAN		Age range 18-34	Age range 60-85
	Female	18 / 26.28 ± 4.43	18 / 68.1 ± 6.67
	Male	19 / 25.57 ± 5.17	14 / 70.16 ± 8.08
	Total	37 / 25.97 ± 4.7	32 / 69.14 ± 7.41
NKI		Age range 18-30	Age range 60-85
	Female	19 / 22.58 ± 2.85	16 / 69.69 ± 7.92
	Male	29 / 22.72 ± 2.81	11 / 70.27 ± 9.3
	Total	39 / 23.08 ± 3.12	27 / 70.29 ± 7.62
Berlin		Age range 18-33	Age range 55-80
	Female	13 / 26 ± 4.73	11 / 64.13 ± 7.74
	Male	12 / 25.33 ± 3.2	3 / 58.75 ± 10.4
	Total	25 / 25.68 ± 4	14 / 62.3 ± 8.71

2 Results on the empirical data analysis

2.1 Graph theoretical metrics of empirical SC and FC network

We did test-retest on three datasets to check the robustness of our observations.

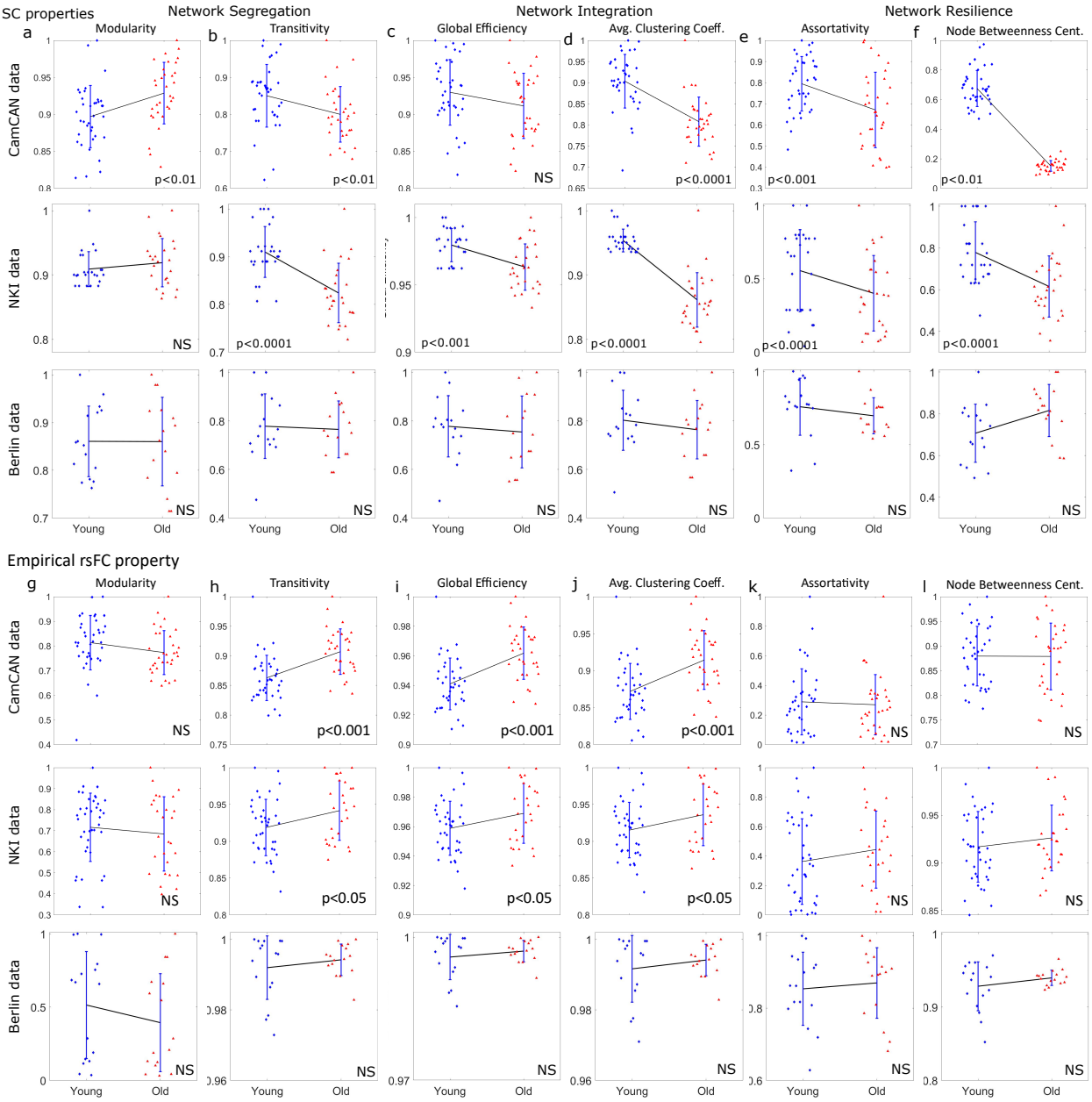

Figure S1 Changes in SC and functional network properties in the three data sets. We joint then by a line to show the pattern of the shift between two means of the two groups. significantly altered or unchanged network properties are determined by two-sample t-test. Number of participants: CamCAN n=37 young, n=32 older adults; NKI n=39 young, n=27 older adults; Berlin n=25 young, n=14 older adults.

2.2 Effect of threshold on empirical rsFC graph properties

The effect of threshold, used to generate binarized FCs, is shown in the Fig. S2. We performed test-retest validation for two different thresholds (corresponds to $p < 0.04, 0.03$ of the correlation matrix, i.e., abs(FC)≥0.085,0.091), which are able to reproduce similar pattern of changes in the graph metrics in the three datasets.

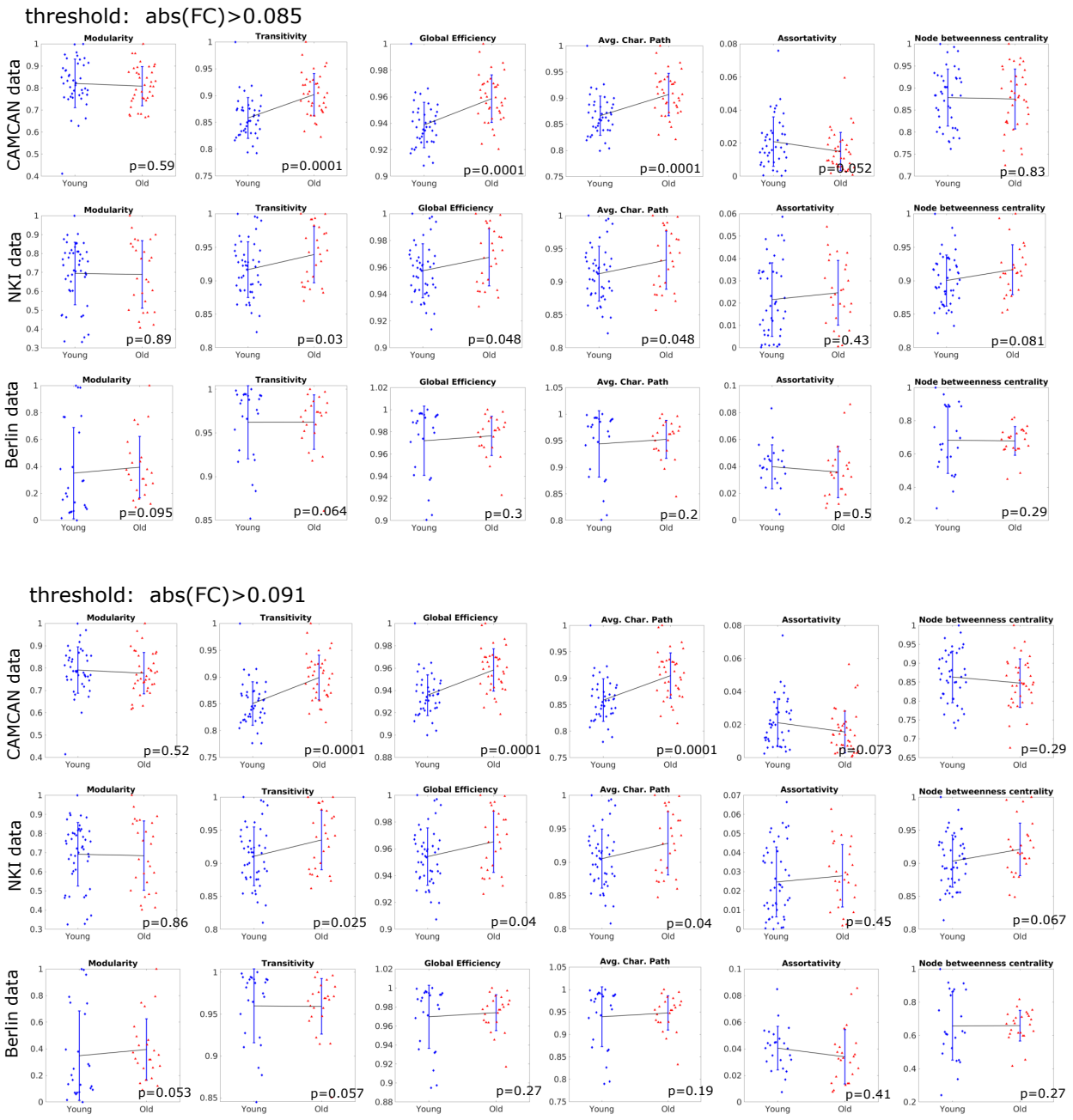

Figure S2 Effect of threshold to binarize the empirical FCs (Pearson correlation coefficient). Patterns of changes in the rsFC network properties in the three datasets remains stable between two age-groups for a wide range of the threshold. Number of participants: CamCAN n=37 young and n=32 older adults; NKI n=39 young and n=27 older adults; Berlin n=25 young and n=14 older adults.

2.3 Consistency of empirical rsFC graph properties

To test the thresholding effects on the FC network property, we defined consistency solely based on our observations on the obtained FC properties for CamCAN and NKI datasets, such that the modularity, assortativity, node-betweenness-centrality are non-significant, whereas, transitivity, global efficiency and average characteristic path are significant when comparing between the two age groups; if any of these conditions are violated we consider as not consistent. We have plotted the graph theoretical metrics (averaged across subjects for each group) against the varying threshold, shown in Fig. S3(a). The three cyan color lines in Fig. S3(a) are the threshold values (0.077, 0.085, and 0.091) used for the empirical rsFC analysis. These three thresholds correspond to the pair-wise p-values (p<0.05, 0.04, and 0.03) obtained during the Pearson correlation coefficient calculation applied to create the FCs from the resting state BOLD signals. Further, to assess

the effect of threshold, we calculate the sparsity and percentage of remaining edges after FC binarization (FC^{bin}), shown in Fig. S3(b). To evaluate sparsity, we introduce the following measure,

$$sparsity = \frac{\text{remaining edges after binarization}}{\text{possible number of edges}} = \frac{\frac{1}{2}\sum_i \sum_j FC_{ij}^{bin}}{n \times (n-1)/2}$$

where, n = total number of brain areas. We also calculate, % of preserved edges = sparsity $\times 100$ %, and edge losses as, loss = [1 − sparsity] $\times$ 100%. The p-values of individual metrics are unified to check the consistency of our observations on FC with varying thresholds. We separated significant and non-significant p-values as: (i) p-values of the metrics showed significant alteration between the two aging cohorts: $p_{sig} = (p\text{val}_\text{T} + p\text{val}_\text{GE} + p\text{val}_\text{CP})/3$, where, $p\text{val}_\text{T}$, $p\text{val}_\text{GE}$ and $p\text{val}_\text{CP}$ represent the p-values computed for the measures transitivity, global efficiency and characteristic path length respectively when comparing between young and old. (ii) p-values of the metrics showed non-significant alteration between the two groups: $p_{nonsig} = (p\text{val}_\text{M} + p\text{val}_\text{A} + p\text{val}_\text{BC}))/3$, where, $p\text{val}_\text{M}$, $p\text{val}_\text{A}$ and $p\text{val}_\text{BC}$ represent the p-values computed for the measures modularity, assortativity and betweenness centrality respectively when comparing between young and older adults. We unified the two outcomes into a single measure, to check the consistency of our observations and amount of edge loss against threshold as, Consistency $= a\Theta(\delta - p_{sig}) + (1-a)\Theta(p_{nonsig} - \delta)$, where, $\Theta(.)$ is the Heaviside function, where δ=0.05 and a=0.5. For visualization purpose, we have inverted the values, showed in Fig. S3(b) in solid blue line. The value becomes 1, only if all the observations are consistent, otherwise 0. Our results are consistent for the loss< 30% edges, where connected component (averaged across subjects) of the graph remains one, as shown in dashed black line. The connected component essentially means every node of a network is accessible at least via one path from any other remaining nodes. We have presented the results choosing the threshold from the shaded range, where the amount of preserved edge is 95% to 84%. The doted-red line and solid yellow lines show preserved edge and loss, respectively.

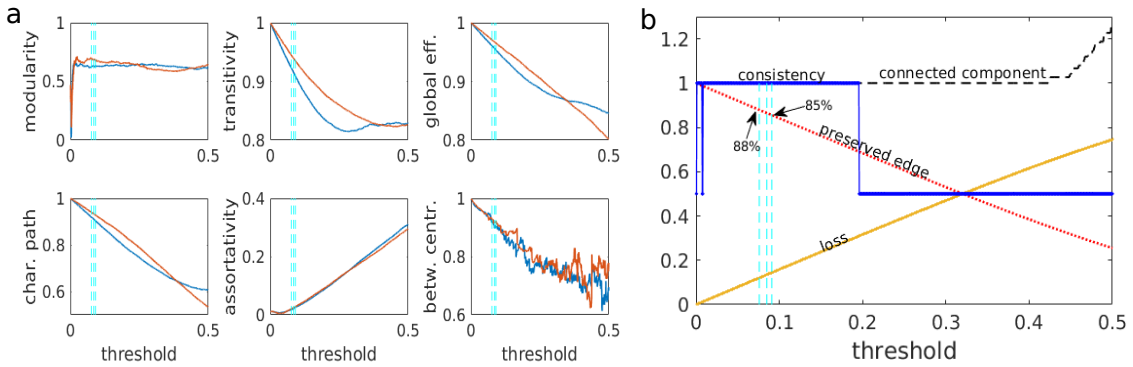

Figure S3 Effects of thresholding on our observations of FC properties are shown for CamCAN data. (a) Graph metrics are shown for varying threshold for young (blue) and old (red). The three cyan color lines are the threshold values ((0.077, 0.085 and 0.091) used to create the binarized empirical rsFC in our analysis. (b) Effects of the thresholding on our observations are measured by consistency, connected component, percentage of edges preserved or lost.

2.4 Empirical BOLD activity at resting state and tasks for CamCAN data

2.4.1 Data sources and participants

The data were collected as part of stage 2 of the Cambridge Centre for Aging and Neuroscience (CamCAN) project (available at http://www.mrc-cbu. cam. ac.uk/datasets/camcan) (Taylor et al (2017); Shafto et al (2014). The fMRI data from resting state [rest] and task periods (naturalistic movie watching [mov] and sensorimotor task [SMT]) were used in the present study.

2.4.2 Data preprocessing

The fMRI data for each functional run (resting state, movie watching, and SMT) were unwarped using fieldmap images, realigned to correct for motion and, slicetime corrected. EPI data were coregistered to the T1 image, transformed to montreal neurological institute (MNI) space using the warps and affine transformation from structural image (estimated using DARTEL). For region of interest (ROI) analysis, mean regional BOLD time series were estimated in 116 parcellated brain areas of Anatomical Automatic Labelling atlas (AAL) Tzourio-Mazoyer et al (2002) (available at http://www.gin.cnrs.fr/tools/aal). Preprocessed data were provided by CamCAN research consortium. Detailed overview of preprocessing pipeline can be found in

Taylor et al (2017). We divided the whole data of 645 participants into two cohorts, young adults with an age range 18-32 years (mean age=26.53 ± 4.09 years), and old adults with an age range 60-88 years (mean age=72.69 ± 7.55 years). Each participant's BOLD time series in the resting state, naturalistic movie watching, and SMTs were utilized to measure the metastability.

2.4.3 Results on empirical metastability in rest and task

Patterns of brain activity appear to be more stable during cognitive operations requiring explicit attention Chen et al (2015); Cohen (2018); Elton and Gao (2015); Hutchison and Morton (2015). Existing theories suggest that spontaneous neural dynamics represent a repository of functional states from which more stable global brain states are constructed during task-based reasoning Alderson et al (2020). Therefore, metastability should be maximal when subjects are at 'rest' and minimal during cognitive demand Alderson et al (2020). We tested the hypothesis that large-scale brain dynamics is more metastable at rest than during the execution of an explicit task. The degree of metastability is shown in Fig. S4 for three conditions, rest, movie watching (mov) and sensory motor task (smt) by considering all participant together (left panel), young cohort (second panel), elderly subjects (third panel), and compare between younger and elderly adults (fourth panel).

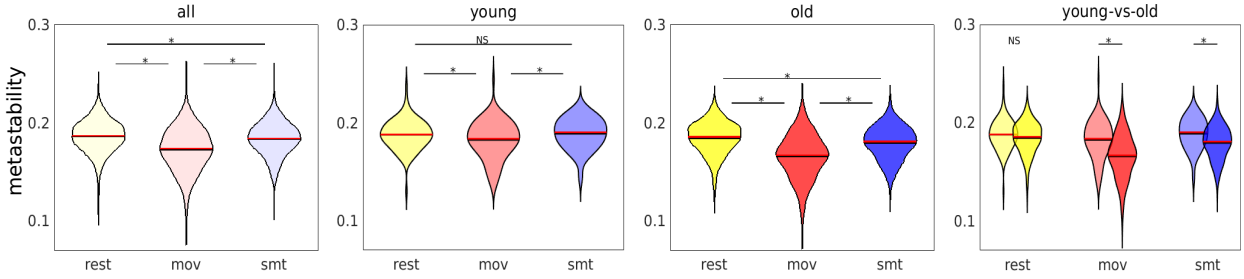

Figure S4 We perform independent t-test to compare empirical metastability for conditions, resting state, movie watching and sensory motor task (n=645 participants). ∗ represents $p<0.01$.

To examine any computational artifacts in our results, we tested our observations against surrogated data using phase randomization, shown in Fig. S5. Lower value of Lin's concordance suggest that the observations from empirical data are not reproducible through any arbitrary or random process.

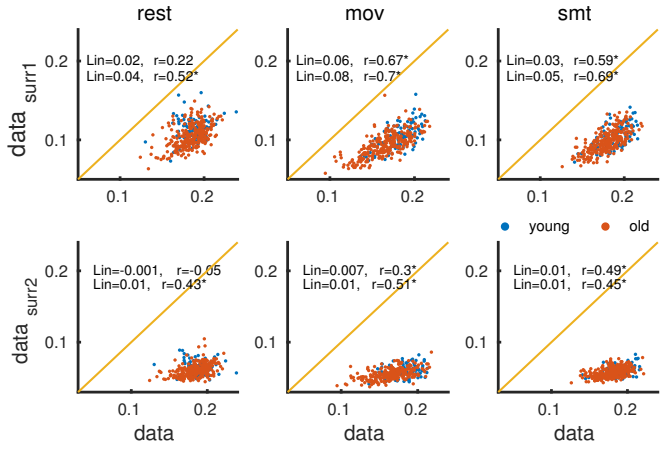

Figure S5 Reproducibility of the empirical metastability from surrogated data (phase randomized BOLD signal). These scatter plots depict the relationships between surrogated and empirical data metastability by Lin's concordance for the CamCAN dataset. Lower values of Lin's concordance suggest that random process is unable to reproduce the empirical metastability in three conditions (resting state, movie watching and sensory motor task) in the two aging cohorts. The texts show Lin's concordance (Lin) and Pearson correlation (r); upper and lower texts for young and older cohort, respectively. ∗ indicates $p<0.01$.

3 Results from the Multiscale Dynamic Mean Field model

3.1 Multiscale Dynamic Mean Field (MDMF) model

The whole-brain dynamics is described by a set of coupled nonlinear stochastic differential equations, the current-based MDMF model Naskar et al (2021) as,

$$
\begin{aligned}
I_i^{(E)} &= w_E I_0 + w_+ J_{NMDA} S_i^{(E)} + G J_{NMDA} \sum_{j=1}^{N} C_{ij} S_j^{(E)} - J_i S_i^{(I)} \\
I_i^{(I)} &= w_I I_0 + J_{NMDA} S_i^{(E)} - c\, S_i^{(I)} \\
r_i^{(E)} &= \frac{a_E I_i^{(E)} - b_E}{1 - exp^{-d_E\left(a_E I_i^{(E)} - b_E\right)}} \\
r_i^{(I)} &= \frac{a_I I_i^{(I)} - b_I}{1 - exp^{-d_I\left(a_I I_i^{(I)} - b_I\right)}} \\
\frac{dS_i^{(E)}}{dt} &= -\beta^E S_i^{(E)} + \alpha^E \left(1 - S_i^{(E)}\right) T_{glu}\; r_i^{(E)} + \sigma \nu_i(t) \\
\frac{dS_i^{(I)}}{dt} &= -\beta^I S_i^{(I)} + \alpha^I \left(1 - S_i^{(I)}\right) T_{gaba}\; r_i^{(I)} + \sigma \nu_i(t)
\end{aligned}
\tag{1}
$$

where, the subscripts i, j indicate brain areas, and superscripts E, I represent excitatory or inhibitory populations, respectively. Total number of considered brain areas is N, where its value is different for different parcellation choice, e.g., $N = 68$ and 188, respectively for Desikan-Killiany parcellation Desikan et al (2006) and Craddock 200 atlas Craddock et al (2012). $S_i^{(E,I)}(t)$ denotes the average excitatory or inhibitory synaptic gating variables at i^{th} local brain area. The time-dependent gating variables are drawn by averaging the fraction of open channels of neurons. The stochasticity is introduced by adding uncorrelated white Gaussian noise ν_i within the equation of two gating variables with intensity σ for each brain region. Further details of the model formulation and descriptions are available in the article by A. Naskar et al. Naskar et al (2021). J_i denotes the local synaptic coupling strength from inhibitory to excitatory. The temporal dynamics of the inhibitory feedback are given by,

$$
\frac{dJ_i}{dt} = \gamma r_i^I (r_i^E - \rho) \tag{2}
$$

At the mean-field level, the biological complexity involved in the balance of dynamics between excitatory and inhibitory fields can be captured grossly using the mathematical implementation of the inhibitory plasticity rule Hellyer et al (2016). An inhibitory plasticity rule represents changes in $J_i(t)$ (synaptic weight) to ensure that the inhibitory current clamps to an excitatory population, maintaining homeostasis. Homeostasis is achieved with $J_i(t)$ dynamics such that the firing rate of the excitatory population is maintained at the target firing rate $\rho = 3Hz$, and γ is the learning rate in *sec*. The chosen target firing rate is the firing rate observed when the inhibitory and excitatory currents are matched.

Table S2 Default parameter values, and descriptions shown with references.

Parameter	Value/Unit	Description	Ref.
I_0	0.382 nA	overall effective external input current	Deco et al (2014)
w_+	1.4	local excitatory recurrence	Deco et al (2014)
J_{NMDA}	0.15 nA	excitatory synaptic coupling strength	Deco et al (2014)
σ	0.001	noise intensity	Naskar et al (2021)
w_E	1	scaling parameter for excitatory populations	Deco et al (2014)
w_I	0.7	scaling parameter for inhibitory populations	Deco et al (2014)
α_E	0.072 $ms^{-1}mMol^{-1}$	forward rate constants of excitatory pools	Destexhe et al (1994)
α_I	0.53 $ms^{-1}mMol^{-1}$	forward rate constants of inhibitory pools	Destexhe et al (1994)
β_E	0.0066 ms^{-1}	backward rate constants of excitatory pools	Destexhe et al (1994)
β_I	0.18 ms^{-1}	backward rate constants of inhibitory pools	Destexhe et al (1994)
a_E	310 nC^{-1}	parameter for input-output function	Deco et al (2014)
a_I	615 nC^{-1}	parameter for input-output function	Deco et al (2014)
b_E	125 Hz	parameter for input-output function	Deco et al (2014)
b_I	177 Hz	parameter for input-output function	Deco et al (2014)
d_E	0.16 s	parameter for input-output function	Deco et al (2014)
d_I	0.087 s	parameter for input-output function	Deco et al (2014)
γ	1 C	learning rate	Naskar et al (2021)
ρ	3 Hz	target firing rate	Deco et al (2014)
G	0.5	global coupling strength	
c	1 nA	local inhibitory to inhibitory strength	
T_{glu}	0.1-15 $mMol$	glutamate concentration	Naskar et al (2021)
T_{gaba}	0.1-15 $mMol$	GABA concentration	Naskar et al (2021)

3.2 Model generated resting-state FC

Here we discussed how we estimate model generated functional connectivity matrix, which will be used to check the model's predictability under certain assumptions. The simulated neural fluctuations were given by the firing rate $r_i^{(E)}(t)$ for i^{th} brain area fluctuates around a fixed value. The neural activity from the MDMF model was converted to the BOLD activity using a hemodynamic Ballon-Windkassel model Friston et al (2003). All the biophysical parameters are taken from Friston et al (2003). The simulated BOLD activity was filtered by a band pass filter and detrending operating converting into normal distribution, while removing trends and temporal mean set to zero for individual brain areas. Pearson correlation between all pair of brain regions generates the resting state model FC.

3.3 Synthetic glutamate-GABA estimation using MDMF model inversion

Figure S6 describes the MDMF model simulation and four steps to estimate model-based concentrations of the two neurotransmitters for a given structural connectivity of individual participants.

Step 1, in Figs. S6(a-d), involves synthetic generation of neural activity and the fitting method that allows us to project the model-generated low frequency $(0.004-0.1\text{Hz})$ BOLD signals and their spatiotemporal harmony, particularly fluctuations in the cortical coherence. The spontaneous brain activity at rest is captured by the empirical BOLD signals derived from resting state fMRI data. The two BOLD signals (empirical and simulated) depict hemodynamic responses of different brain areas, where pair-wise spatial correlation is the weights in the functional connectivity (FC) matrix. Detailed steps in the first stage analysis are: Fig. S6(a) We use anatomical connectivity derived from diffusion tensor imaging from the subjects of different ages. Fig. S6(b) A mean-field neuronal model is put on top of the structural connectivity matrix. Thus, the nodal dynamics is governed by the MDMF model Naskar et al (2021) and spatially connected via SC matrix. The structural connectivity describes the inter-areal interaction strength to exchange excitability across the cortical regions. We generate a model simulated neural activity, firing rate of excitatory/inhibitory populations of individual regions. The Balloon-Windkessel algorithm Friston et al (2003) then estimates the hemodynamic activity at rest. A Pearson correlation is derived from the estimated hemodynamic activity between each pair of brain regions. Thus, we approximate the functional connectivity (FC), which we mentioned as the model based or simulated FC. Figure S6(c) shows an exemplary resting-state fMRI activation map, which is used

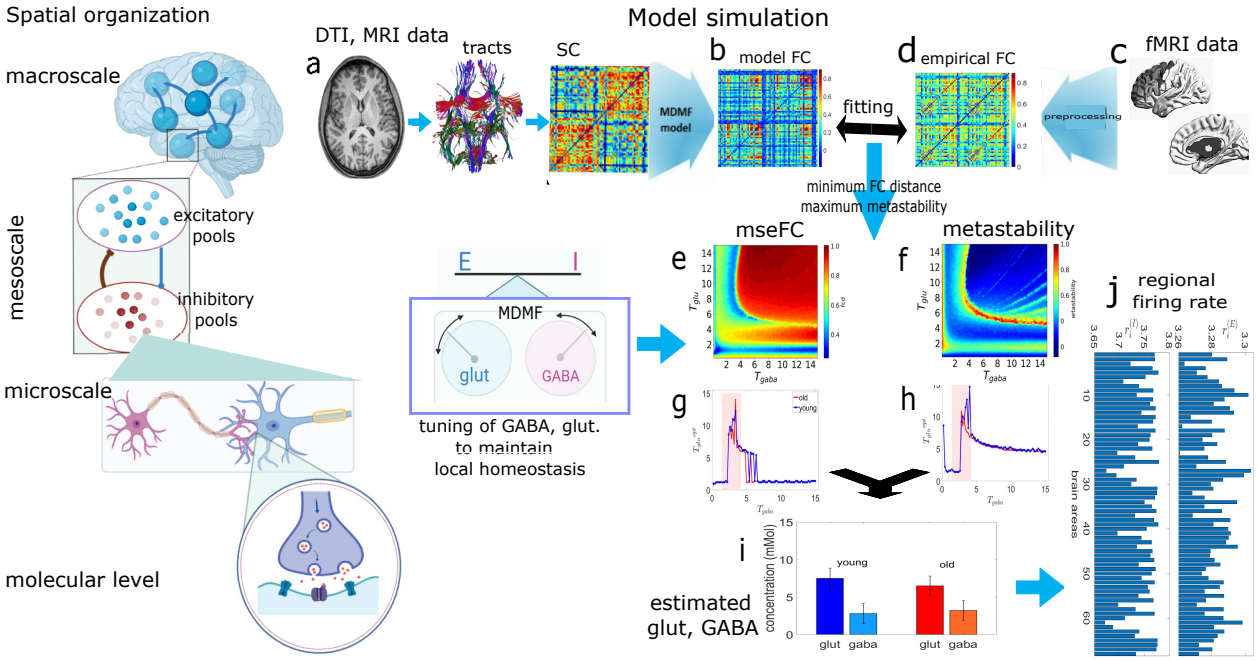

Figure S6 Estimation of synthetic GABA and glutamate using MDMF model. Four steps of the model simulation and synthetic result generation are shown here. (a-d) Step 1, we compare the model FC from spatiotemporal patterns to those observed in the empirical FC obtained from fMRI BOLD activity at rest. (e, f) In step 2, mseFC and metastability are stored for each pair of GABA-glutamate values. (g, h) Step 3, we estimate optimal glutamate for different values of GABA imposing the two optimal conditions. (i) Step 4, an optimal GABA is estimated from the result obtained in the previous step. Thus, an optimal set of GGC is estimated for an individual subject, based on mseFC and metastability measures. Few icons and assets are taken from the biorender (Created in https://BioRender.com).

to extract empirical resting-state BOLD activity of individual subjects using CONN toolbox. In Fig, S6(d), we plot the empirical rsFC from the BOLD activity, which is used in fitting against resting-state model FC.

In Step 2, the fitting measures Euclidean distance between empirical and model FCs, called mean square root error between two functional connectivity (mseFC), shown in Fig. S6(e). Simultaneously, the fluctuation in global coherence is measured by metastability, when tuning the two intrinsic parameters (T_{glu} and T_{gaba}), see Fig. S6(f). We have varied the two local parameters, T_{glu} and T_{gaba} homogeneously across the whole brain and store the two measures for each pair of parameter values in the two-parameter phase diagrams, see Figs. S6(e) and S6(f).

In Step 3, see Figs. S6(g, h), we scan along the x-axis, i.e., across GABA values, and estimate optimal glutamate concentration (T_{glu}) in $mMol$ imposing two optimal conditions, minimum FC distance (i.e., maximum correlation between the model-generated FC and empirical rsFC), and maximum metastability, which decides optimal brain functionality. We average over the estimated glutamate values obtained from the two measures from Figs. S6(g, h).

Finally, in Step 4, GABA concentration is estimated for the homeostasis range Naskar et al (2021), indicated by shaded boxes in Figs S6(g, h) under the same optimal conditions. Thus, subject-wise optimal parameter set of T_{gaba} and T_{glu}, is predicted investigating whole-brain neuroimage data (MRI, fMRI), shown using a representative result in Fig. S6(i). The firing rate remains at the desired set point of ∼4Hz, as shown in Fig. S6(j), only for the optimal choice of the neurotransmitter levels.

Further, we monitor GABA-glutamate concentrations (GGC) and their ratio (GGR) for two aging cohorts at the level of single subjects. We separate healthy subjects into two discrete age groups, young and old. Then, a possible alteration (or invariance) pattern in the two metabolites is captured over the lifespan, which has helped draw a plausible conclusion.

3.4 Model performance evaluation: Effects of thresholds on simulated FC graph properties

We perform test-retest validation to examine the effect of the threshold used to binarize the simulated FCs, generated considering optimal GABA-glutamate values, presented in Fig. S7. We present the results obtained

for two different thresholds, which are able to reproduce a similar pattern of changes in the graph metrics in the two datasets. We refer to Fig. S1 and Fig. S2 for empirical rsFC properties to compare the pattern of age-related changes in the graph metrics against the results obtained in simulated FCs, shown in Fig. S7. The node betweenness centrality is not fully predicted by the model, though other network properties have behaved similarly to those of empirical data. Due to fewer participants in the Berlin dataset in two groups, we did not perform the training and testing simulations to assess the network properties.

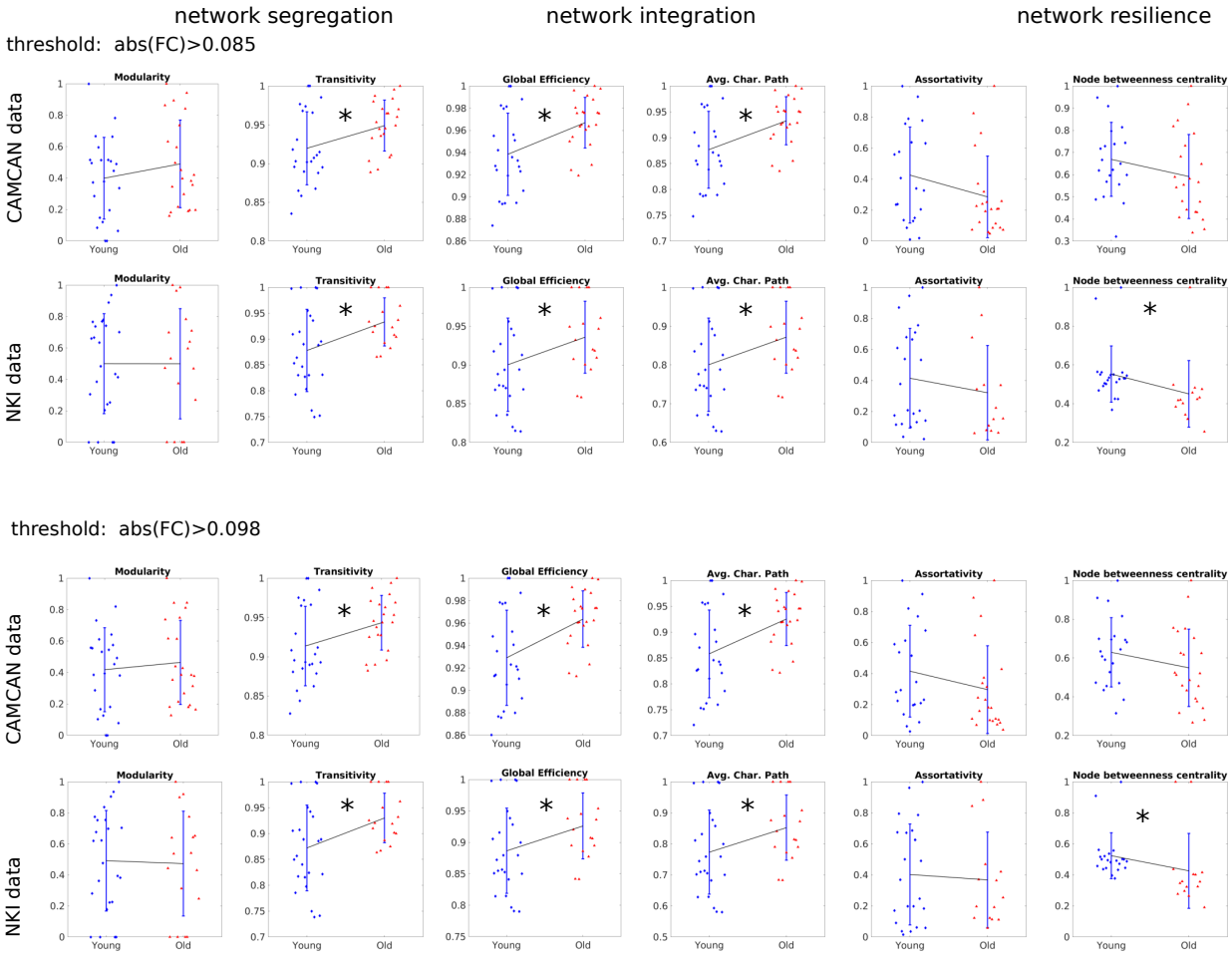

Figure S7 Effect of threshold to binarize the simulated FCs. The pattern of changes between young and old cohorts in the model-based FCs properties remains almost similar to that of empirical rsFC properties for a wide range of the threshold. Only node betweenness centrality metric is not fully predicted in the test cohorts; while comparing between the age groups, the statistical significance does match to the empirical observation. $*$ represents $p < 0.05$, otherwise not significant.

3.5 Effect of coupling strength on the GABA/glutamate estimation

Figure S8 shows the fitting for coupling strength in CamCAN data in the top row. We use FC-FC correlation, distance between empirical and simulated FCs, and FC dynamics (FCD) distance, as well. The estimated parameters are presented for various coupling strengths in the second row, whereas corresponding firing rates are presented in the third and fourth rows. The simulated FCs for both young and older adults are generated based on the estimated GABA/glutamate values, shown in the last two rows in Fig. S8. Within the shaded region, we have observed a similar pattern of Glutamate/GABA changes between the two age groups.

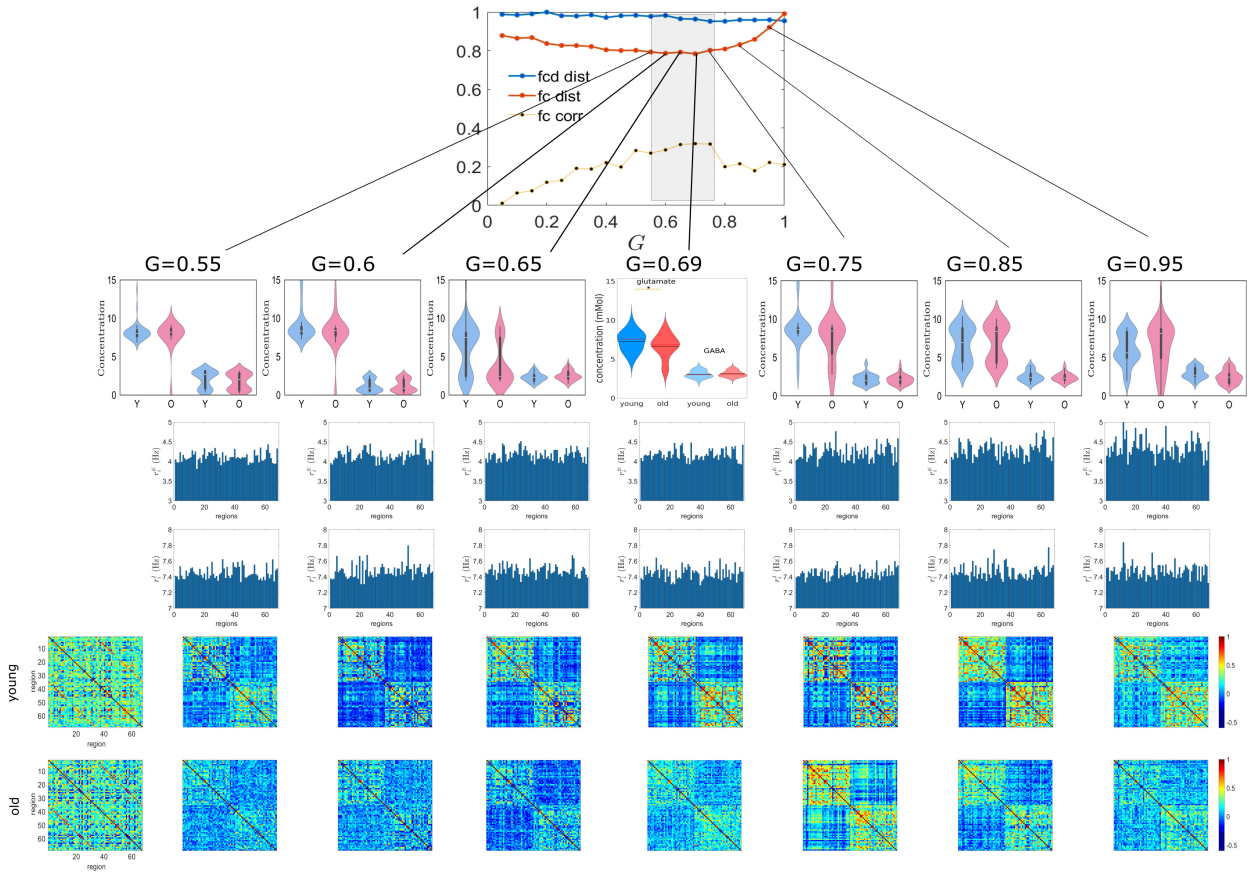

Figure S8 Effect of coupling strength (G) on parameter estimation and firing rates. The results are produced in CamCAN data. The top panel shows fitting of the coupling strength based on the distance and correlation between static FCs, and also dynamic FC distance. We have selected G=0.69 for our analysis in CamCAN data (young n=37, old n=32). Second row shows optimal GABA/Glutamate estimated at different G values. In the shaded range, we observe a similar pattern of age-related neurotransmitter changes. Excitatory and inhibitory firing rates obtained for a single participant are plotted in the third and fourth rows, respectively. The fifth and last rows present empirical and simulated FCs from one young adult and elderly participant, generated for different G values. Simulated FC is not the best fit and excitatory firing activity fluctuates at much higher rate when G is higher than optimal value.

References

Alderson TH, Bokde AL, Kelso JS, et al (2020) Metastable neural dynamics underlies cognitive performance across multiple behavioural paradigms. Human brain mapping 41(12):3212–3234

Andersson JL, Skare S, Ashburner J (2003) How to correct susceptibility distortions in spin-echo echo-planar images: application to diffusion tensor imaging. Neuroimage 20(2):870–888

Brown J, et al (2012) The ucla multimodal connectivity database: a web-based platform for brain connectivity matrix sharing and analysis. Frontiers in Neuroinformatics 6:28

Chen B, Xu T, Zhou C, et al (2015) Individual variability and test-retest reliability revealed by ten repeated resting-state brain scans over one month. PloS one 10(12):e0144963

Cohen JR (2018) The behavioral and cognitive relevance of time-varying, dynamic changes in functional connectivity. NeuroImage 180:515–525

Craddock RC, James GA, Holtzheimer III PE, et al (2012) A whole brain fmri atlas generated via spatially constrained spectral clustering. Human Brain Mapping 33(8):1914–1928

Dale AM, Fischl B, Sereno MI (1999) Cortical surface-based analysis: I. segmentation and surface reconstruction. Neuroimage 9(2):179–194

Deco G, Ponce-Alvarez A, Hagmann P, et al (2014) How local excitation–inhibition ratio impacts the whole brain dynamics. Jour of Neuroscience 34(23):7886–7898

Desikan RS, Ségonne F, Fischl B, et al (2006) An automated labeling system for subdividing the human cerebral cortex on mri scans into gyral based regions of interest. Neuroimage 31(3):968–980

Destexhe A, Mainen ZF, Sejnowski TJ (1994) Synthesis of models for excitable membranes, synaptic transmission and neuromodulation using a common kinetic formalism. Journal of Computational Neuroscience 1(3):195–230

Dhollander T, Raffelt D, Connelly A (2018) Accuracy of response function estimation algorithms for 3-tissue spherical deconvolution of diverse quality diffusion mri data. In: Proceedings of the Joint Meeting of the European Society for Magnetic Resonance in Medicine and Biology and the International Society of Magnetic Resonance in Medicine, Paris, France

Elton A, Gao W (2015) Task-related modulation of functional connectivity variability and its behavioral correlations. Human brain mapping 36(8):3260–3272

Friston KJ, Harrison L, Penny W (2003) Dynamic causal modelling. Neuroimage 19(4):1273–1302

Hellyer PJ, Jachs B, Clopath C, et al (2016) Local inhibitory plasticity tunes macroscopic brain dynamics and allows the emergence of functional brain networks. NeuroImage 124:85–95

Hutchison RM, Morton JB (2015) Tracking the brain's functional coupling dynamics over development. Journal of Neuroscience 35(17):6849–6859

Kellner E, Dhital B, Kiselev VG, et al (2016) Gibbs-ringing artifact removal based on local subvoxel-shifts. Magnetic resonance in medicine 76(5):1574–1581

Mori S, Van Zijl PC (2002) Fiber tracking: principles and strategies–a technical review. NMR in Biomedicine: An Int Jour Devoted to the Devel and Appl of Magnetic Resonance In Vivo 15(7-8):468–480

Naskar A, Vattikonda A, Deco G, et al (2021) Multi-scale dynamic mean field model (mdmf) relates resting-state brain dynamics with local cortical excitatory–inhibitory neurotransmitter homeostasis. Network Neuroscience pp 1–55

Schirner M, Rothmeier S, Jirsa VK, et al (2015) An automated pipeline for constructing personalized virtual brains from multimodal neuroimaging data. NeuroImage 117:343–357

Shafto MA, Tyler LK, Dixon M, et al (2014) The cambridge centre for ageing and neuroscience (cam-can) study protocol: a cross-sectional, lifespan, multidisciplinary examination of healthy cognitive ageing. BMC neurology 14(1):1–25

Smith RE, Tournier JD, Calamante F, et al (2012) Anatomically-constrained tractography: improved diffusion mri streamlines tractography through effective use of anatomical information. Neuroimage 62(3):1924–1938

Smith RE, Tournier JD, Calamante F, et al (2015) Sift2: Enabling dense quantitative assessment of brain white matter connectivity using streamlines tractography. Neuroimage 119:338–351

Taylor JR, Williams N, Cusack R, et al (2017) The cambridge centre for ageing and neuroscience (cam-can) data repository: Structural and functional mri, meg, and cognitive data from a cross-sectional adult lifespan sample. neuroimage 144:262–269

Tournier JD, Smith R, Raffelt D, et al (2019) Mrtrix3: A fast, flexible and open software framework for medical image processing and visualisation. Neuroimage 202:116137

Tustison NJ, Avants BB, Cook PA, et al (2010) N4itk: improved n3 bias correction. IEEE transactions on medical imaging 29(6):1310–1320

Tzourio-Mazoyer N, Landeau B, Papathanassiou D, et al (2002) Automated anatomical labeling of activations in spm using a macroscopic anatomical parcellation of the mni mri single-subject brain. Neuroimage 15(1):273–289

Veraart J, Novikov DS, Christiaens D, et al (2016) Denoising of diffusion mri using random matrix theory. Neuroimage 142:394–406

Whitfield-Gabrieli S, Nieto-Castanon A (2012) Conn: a functional connectivity toolbox for correlated and anticorrelated brain networks. Brain connectivity 2(3):125–141